BBA - Molecular Basis of Disease 1871 (2025) 167569

Contents lists available at ScienceDirect

BBA - Molecular Basis of Disease

journal homepage: www.elsevier.com/locate/bbadis

CRISPR-Cas9 mediated knockout of *NDUFS4* in human iPSCs: A model for mitochondrial complex I deficiency

Shivani Goolab [a,1], Karin Terburgh [b,1], Charl du Plessis [b], Janine Scholefield [a,c,d], Roan Louw [b,*]

[a] Bioengineering and Integrated Genomics Group, Future Productions: Chemicals Cluster, Council for Scientific and Industrial Research, Pretoria, South Africa
[b] Human Metabolomics, Faculty of Natural and Agricultural Sciences, North-West University, Potchefstroom, South Africa
[c] Department of Human Biology, Faculty of Health Sciences, University of Cape Town, Cape Town, South Africa
[d] Division of Human Genetics, Faculty of Health Sciences, University of the Witwatersrand, Johannesburg, South Africa

ARTICLE INFO

Keywords:
iPSC
CRISPR-Cas9
Mitochondrial disease
CI deficiency

ABSTRACT

Mitochondrial diseases, often caused by defects in complex I (CI) of the oxidative phosphorylation system, currently lack curative treatments. Human-relevant, high-throughput drug screening platforms are crucial for the discovery of effective therapeutics, with induced pluripotent stem cells (iPSCs) emerging as a valuable technology for this purpose. Here, we present a novel iPSC model of *NDUFS4*-related CI deficiency that displays a strong metabolic phenotype in the pluripotent state. Human iPSCs were edited using CRISPR-Cas9 to target the *NDUFS4* gene, generating isogenic *NDUFS4* knockout (KO) cell lines. Sanger sequencing detected heterozygous biallelic deletions, whereas no indel mutations were found in isogenic control cells. Western blotting confirmed the absence of NDUFS4 protein in KO iPSCs and CI enzyme kinetics showed a ~56 % reduction in activity compared to isogenic controls. Comprehensive metabolomic profiling revealed a distinct metabolic phenotype in *NDUFS4* KO iPSCs, predominantly associated with an elevated NADH/NAD^+ ratio, consistent with alterations observed in other models of mitochondrial dysfunction. Additionally, β-lapachone, a recognized NAD^+ modulator, alleviated reductive stress in KO iPSCs by modifying the redox state in both the cytosol and mitochondria. Although undifferentiated iPSCs cannot fully replicate the complex cellular dynamics of the disease seen *in vivo*, these findings highlight the utility of iPSCs in providing a relevant metabolic milieu that can facilitate early-stage, high-throughput exploration of therapeutic strategies for mitochondrial dysfunction.

1. Introduction

Mitochondrial diseases pose significant challenges in preclinical and clinical studies as they exhibit a wide range of genetic and clinical heterogeneity, show tissue-specific susceptibility, and lack validated disease-modifying therapies [1–3]. While primary mitochondrial diseases are considered rare, mitochondrial dysfunction has been documented in more prevalent conditions, including psychiatric disorders [4,5], neurodegenerative diseases [6–8], and diabetes [9,10]. These complex metabolic disorders frequently present with deficiencies in complex I (CI) of the oxidative phosphorylation system [11–14].

CI, also known as NADH-ubiquinone oxidoreductase (EC 1.6.5.3), cycles NADH to NAD^+, transferring electrons to ubiquinone, and generating the largest portion of the proton motive force necessary for ATP production in mitochondria [14,15]. Isolated CI deficiency is associated with mutations in over 38 genes [16], with >17 loss-of-function mutations identified in the nuclear NADH-dehydrogenase subunit S4 (*NDUFS4*) gene — rendering *NDUFS4* a mutational hotspot for CI deficiency [17–19]. *NDUFS4*, situated on chromosome 5q11.2, comprises 5 exons in its coding region, which are translated into the 175-amino acid NDUFS4 pre-protein, that includes a 42-amino acid mitochondrial targeting sequence (MTS) (Fig. 1a) [20,21]. As an accessory subunit of CI, NDUFS4 is essential for the assembly, stability, and activity of the 45-subunit complex [22,23].

To gain deeper insight into *NDUFS4*-related CI deficiency, a diverse array of models has been developed [24]. To date, *Ndufs4* knockout (KO) mice, which display a primarily neurological phenotype, remain one of the most extensively studied preclinical models that closely resemble symptoms of human CI deficiency [6,25]. While mouse models offer valuable insight into physiologically complex diseases, they have

* Corresponding author.
E-mail address: Roan.Louw@nwu.ac.za (R. Louw).
[1] co-first authors.

https://doi.org/10.1016/j.bbadis.2024.167569
Received 31 May 2024; Received in revised form 5 November 2024; Accepted 6 November 2024
Available online 14 November 2024

limitations for high-throughput drug screening. Breeding and treatment are resource-intensive, time-consuming, and pose considerable ethical challenges for large-scale use. Advances in human induced pluripotent stem cell (iPSCs) and gene editing technologies effectively mitigate many of these challenges [26–28].

IPSCs have gained traction in disease modelling owing to their ability to self-renew almost indefinitely and differentiate into diverse cell types whilst retaining the inherent genetic diversity of the donor [29]. IPSCs are generated by reprogramming somatic cells, which is achieved by rewiring the chromatin landscape to ensure endogenous expression of master regulators of stemness through the overexpression of specified transcription factors [30]. When using iPSCs to model monogenic diseases, it is imperative to create isogenic control lines that provide a matched genetic background for the detection of subtle phenotypic differences [31]. Clustered regularly interspaced short palindromic repeats (CRISPR) [32-35] has advanced the efficiency and ease of developing isogenic cellular models [33] by either correcting pathogenic mutations from patient-derived iPSCs, or recreating these mutations in normal iPSCs. In this regard, the most common strategy utilized involves the introduction of insertions/deletions (indels), which may result in frame shift mutations and consequently the synthesis of a truncated protein, a common strategy to produce a functional KO [31,34–36].

While iPSC-derived models have been used extensively to recapitulate disease phenotypes *in vitro* [29], they do not fully replicate the complexity of *in vivo* disease models. iPSCs do, however, offer a human-based platform that enables rapid, scalable studies, complementing traditional animal models. Including *in vitro* and *in vivo* models across multiple, distinct species in the drug discovery process greatly increases the rigor and translatability of pre-clinical studies for complex diseases such as mitochondrial disease [37]. The FDA Modernization Act 2.0 [38], which no longer mandates animal testing for all drugs before clinical trials, further encourages the use of human-relevant *in vitro* models, such as iPSCs to shorten pre-clinical drug discovery timelines, reduce reliance on animal testing, and enhance the likelihood of success in clinical trials.

Several groups have started modelling mitochondrial disease [28], including *NDUFS4*-related CI deficiency [39–41], using iPSCs and CRISPR technology. For the most part, these iPSC lines were differentiated into physiologically relevant model systems with which to investigate cellular pathway disruption and provide a potential cellular screening tool. However, recent studies have demonstrated the utility of undifferentiated iPSCs for drug screening [42,43]. In this context, we developed, characterized, and metabolically investigated *NDUFS4* KO iPSCs in their pluripotent state.

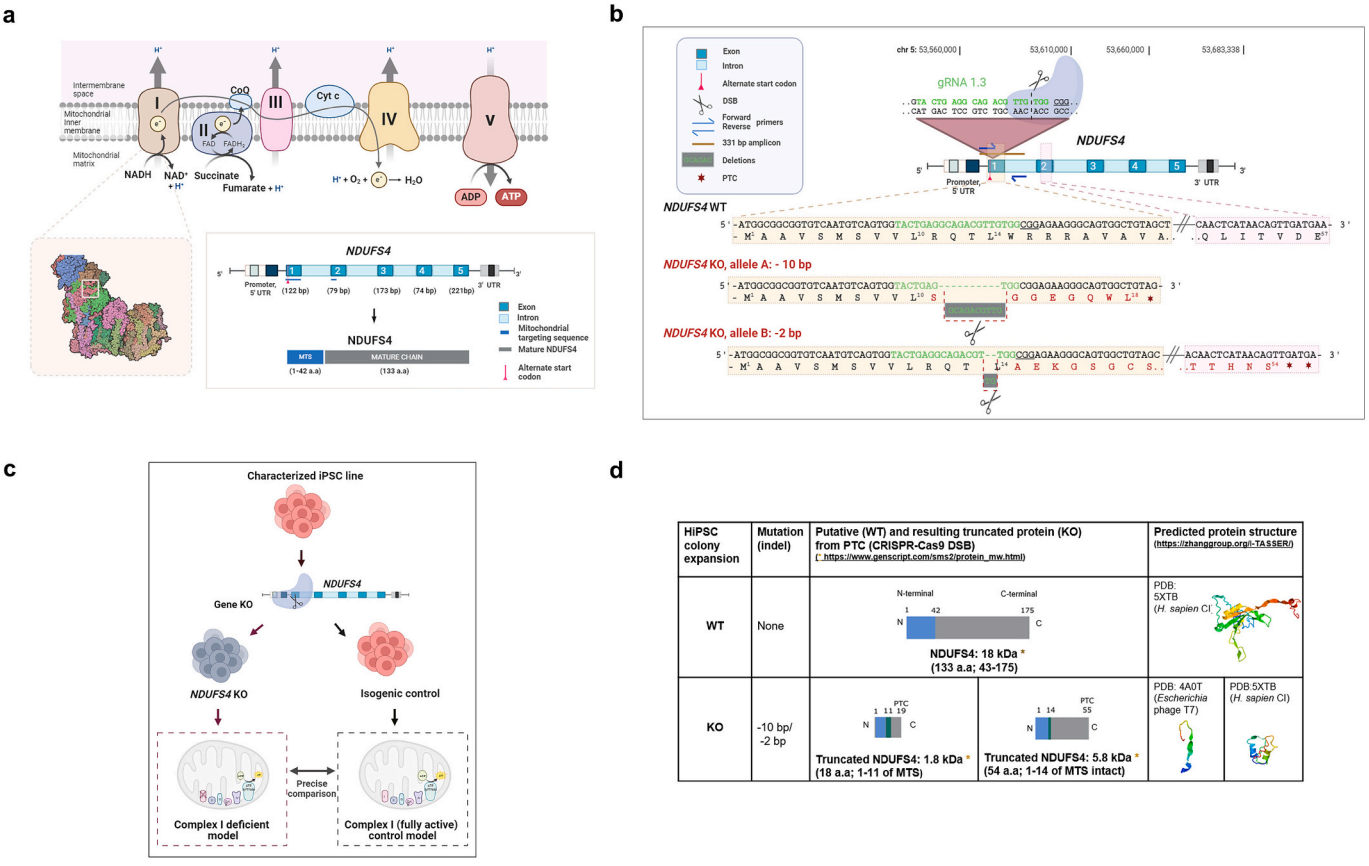

Fig. 1. Generation of an iPSC-based model of CI deficiency due to *NDUFS4* KO by CRISPR-Cas9. (a). Mitochondrial respiratory chain, the localization of the NDUFS4 subunit in human respiratory complex I (RCSBPDB:5XTD), and the NDUFS4 pre-protein with its encoding gene containing an alternate initiation codon. (b) Genome editing approach used to KO NDUFS4, by introducing a frameshift mutation within the coding region of the biallelic KO in comparison to the isogenic control line WT (absence of deletion). Scissors: cut site, blue arrows: primers to amplify mutation site, grey box: deletion mutations, and red stars: PTC. (c) Application of iPSCs and CRISPR-Cas9 to produce a CI deficient mitochondrial model and the isogenic control to enable the precise phenotypic comparison (by negating the variation from different genetic background). (d) Overview of putative and resultant protein truncation and predicted protein structures of WT and KO lines (clones), respectively. Blue box: MTS, dark green box: altered amino acid residues, and grey box: conserved amino acid residues in comparison to the putative sequence. Ribbon diagrams are assigned according to rainbow coloring with blue depicting the N-terminal position to red depicting the C-terminal position. *Abbreviations: a.a., amino acid; CI, complex I; CoQ, coenzyme Q; Cyt c, cytochrome C; gRNA, guide RNA; DSBs, double strand breaks; KO, knockout; iPSC, human induced pluripotent stem cell; MTS, mitochondrial targeting sequence; PTC, premature termination codon; Seq, sequence; UTR, untranslated region; WT, wildtype.* (For interpretation of the references to colour in this figure legend, the reader is referred to the web version of this article.)

2. Materials and methods

2.1. Fibroblast cell culture

Human dermal fibroblasts (HDFs), mouse embryonic fibroblasts (MEFs) and PLAT-GP retrovirus producing cells were cultured at 37 °C with 5 % CO_2 in HDF medium comprising Dulbecco's modified eagle medium (DMEM) containing 10 % fetal bovine serum (FBS), 1 mM GlutaMax, 1 % nonessential amino acids (NEAA), 50 μM β-mercaptoethanol (βME) and 1 % Pen-strep (penicillin and streptomycin). HDF medium was replaced every alternative day.

2.2. iPSC generation and characterization

HDFs from a female of African descent were purchased from Lonza Biosciences (Switzerland). HDFs were reprogrammed into iPSCs within six passages by retrovirus transduction as previously described [30]. Briefly, the following plasmids pMXs-hOCT3/4 (Addgene plasmid # 17217), pMXs-hSOX2 (Addgene plasmid # 17218), pMXs-hKLF4 (Addgene plasmid # 17219), and pMXs-hc-L-MYC (Addgene plasmid # 17220) [30] were used to create retrovirus for transduction. Six days post transduction, cells were seeded on 0.1 % gelatin coated culture plates under feeder layer conditions (iMEFs) [44,45] with daily medium changes using human embryonic stem cell medium (hESC) or MEF-conditioned medium. Both media were supplemented with 10 ng/mL human basic fibroblast growth factor (bFGF) and 55 μM βME. The hESC medium consisted of DMEM/F12, 20 % KnockOut™ Serum Replacement (KSR), 1 % NEAA, 1 mM GlutaMax, 1 % Pen-strep, 10 ng/mL bFGF and 50 μM βME. Approximately four weeks after transduction, the iPSC colonies with correct morphology were expanded by mechanical dissociation, and after 10 passages, were shifted to feeder-free conditions as outlined in Section 2.7.

2.3. Indirect immunocytochemistry

To confirm the expression of pluripotency markers (SSEA-4, Oct4, and Nanog), iPSC colonies after 10 passages were fixed, permeabilized, followed by binding of primary and secondary antibodies [30], and nuclei staining with DAPI.

2.4. Quantitative PCR (qPCR) of endogenous and exogenous genes

RNA was isolated using the Direct-Zol RNA Kit according to the manufacturer's instruction from the HDF prior to transduction, iPSCs, and HDF expressing exogenous genes (Oct4, Sox2, and Klf4). QPCR analysis was used to confirm transgene silencing after retroviral transduction and was performed as previously described [30]. Briefly, cDNA was synthesized using SuperScript II reverse transcriptase (Invitrogen) according to the manufacturer's instructions. QPCR was performed with SYBR Green (BioRad) and analyzed using the CFX96 real-time qPCR system (BioRad) according to the manufacturer's instructions. Nanog and β-actin were assayed as a pluripotency marker and a control for mRNA quality, respectively.

2.5. Karyotyping

Chromosomal G-band [46] and copy number variant [47] analyses were used to confirm genomic integrity.

2.6. In vitro germ layer differentiation

Embryoid bodies were formed as previously described [48] to confirm the differentiation capacity of iPSCs into the embryonic germ layers (endoderm, mesoderm, and ectoderm) by indirect immunocytochemistry [30].

2.7. Cell maintenance and harvesting

IPSCs were cultured under feeder-free conditions at 37 °C with 5 % CO_2 in Geltrex™-coated vessels using CTS™ Essential 8™ (E8) medium. Cells were seeded at a density of 2–4 × 10^4 cells/cm^2, with daily medium changes, and subcultured every 3–5 days. All liquids were pre-warmed to 22 °C before use. To enhance single-cell survival, E8 medium was supplemented with 10 μM Y-27632 dihydrochloride during cell thawing, harvesting, and the first 24 h after subculturing. Cells were passaged at 70–75 % confluency for subculturing using CTS™ TrypLE™ according to the manufacturer's instructions.

2.8. Culturing cells with β-lapachone

KO iPSCs were cultured in T25 culture flasks, with and without 0.05 μM β-lapachone (βL; 3,4-dihydro-2,2-dimetyl-2H-naphthol[1,2-*b*]pyran-5,6-dione). In short, βL was dissolved in DMSO (1 mM) and diluted in E8 medium to 0.05 μM. KO cells were cultured with/without βL for 24 h, with all cells receiving equivalent DMSO concentrations. After the incubation, cells were harvested and the metabolites extracted as described in Section 2.18 before specific redox marker metabolites were measured using the GC–MS/MS method described in Section 2.18.

2.9. CRISPR Cas9-gRNA plasmid construction

The Cas9-gRNA expression vector was constructed by inserting annealed oligonucleotides into the *Bbs*I-cleaved pX330 plasmid (Addgene plasmid #42230). The online tool, CRISPOR [49], was used to select three high-performance gRNAs based on high efficiency, which targeted the first exon of *NDUFS4* and was located downstream of the second ATG codon. This computational tool, at the time of gRNA design, made use of the existing reference genome, which does not account for all genetic variants common in underrepresented populations. The gRNA that mediated the highest indel efficiency based on the T7 endonuclease I (T7E1) mismatch cleavage assay was selected for iPSC transfection.

gRNA 1.3 sequence- 5′- TACTGAGGCAGACGTTGTGG -3′.

2.10. iPSC transfection

iPSCs were transfected at 70–80 % confluence using Lipofectamine Stem reagent in 24-well tissue culture plates. For each transfection experiment, 0.75 × 10^5 cells were transfected with 2 μL Lipofectamine Stem reagent and 2 μg of plasmid DNA (pX330), which coexpressed Cas9 and the target gene-specific gRNA 1.3. Ninety-six hours after transient expression of the Cas9-gRNA components, cells were dissociated reserving 40 % of iPSC cell pellet for genomic DNA extraction and 60 % for cryopreservation in equivalent volumes of iPSC freezing medium A (60 % Knockout™ DMEM: 40 % Knockout™ Serum Replacement) and iPSC freezing medium B (80 % Knockout™ DMEM, 20 % DMSO).

2.11. Genomic DNA extraction and PCR

Human gDNA was extracted from iPSCs and derived, edited clones using the PureLink® Genomic DNA Kits according to the manufacturer's instructions. The *NDUFS4* target sequence was amplified from iPSC gDNA using Phusion™ High–Fidelity DNA Polymerase according to the manufacturer's instructions.

Primer sequence:

NDUFS4-1F 5′- CTGGCTTGAGAACGAAGGAAG -3′.

NDUFS4-1R 5′- CCATTGATAGCAGACAGTCCCT -3′.

2.12. Indel efficiencies of an edited iPSC population assessed by T7 endonuclease I assay (T7E1)

The genomic locus targeted by Cas9 was amplified, PCR purified using the GeneJET PCR purification kit, and the PCR amplicons were

subjected to repeated denaturation and re-annealing cycles as described previously [34,35,50,51]. The mismatched DNA sequences that generated heteroduplexes were cleaved by T7E1 and the cleaved products were resolved on a 12 % (*v*/v) acrylamide gel. Semi-quantification of band intensities obtained for uncleaved homoduplexes and cleaved heteroduplexes were performed using the FIJI software [52].

2.13. Isolation of iPSC clones and indel assessment

The global edited iPSC population was seeded in single cells by repeat triturating through a 70 μM Corning® cell strainer at 2000 cells in a 60.1 cm^2 culture plate and expanded for seven days. Individual emerging colonies were manually picked, transferred to 96-well culture plates, and expanded to 60–90 % confluency. The genomic locus mutated by Cas9 was amplified by PCR and the purified PCR amplicons were denatured and re-annealed as previously described [34,35,50,51]. The reannealed product was treated with crude Cel1 extract [53,54] and the reactions were incubated at 45 °C for 7 min followed by a spike with the crude Cel1 extract and further incubation at 45 °C for 8 min. Edited and isogenic control iPSC colonies positively screened by Cel1 endonuclease were sequenced and frameshift mutations were confirmed as shown in Fig. S1b. The mutational status of the alleles in the iPSC clones was further evaluated by subcloning the amplified region into a bacterial cloning plasmid and individual bacterial colonies were sequenced. Local alignments of the DNA sequences originating from the isogenic and edited, biallelic KO clones near the region of interest, the expected double-strand break (DSB), were compared (Fig. S1c).

2.14. Mitochondrial fraction preparation for protein analyses

Mitochondria-enriched fractions were prepared from iPSCs by differential centrifugation. For each analysis, three replicate samples (*i.e.* distinct cultures in parallel) were prepared per genotype. Each cell pellet, harvested from a T75 culture flask, was washed three times with chilled PBS before being resuspended in chilled Zheng buffer (pH 7.2; 210 mM mannitol, 70 mM sucrose, 5 mM HEPES free acid, and 0.1 mM EGTA) and homogenized using a Dounce tissue grinder through 30 strokes with a small clearance pestle. Homogenates were centrifuged at 600 ×*g* (10 min, 4 °C), with the resulting supernatant centrifuged at 16000 ×*g* (20 min, 4 °C) to obtain a mitochondria-enriched pellet. Mitochondrial fractions were then resuspended in an appropriate solvent, based on subsequent analysis, before storage at −20 °C. For SDS-PAGE, mitochondrial fractions were resuspended in chilled 0.86× RIPA cell lysis buffer (pH 8.0) containing 1× cOmplete™ Mini EDTA-free protease inhibitor cocktail and 0.1 % (*v*/v) Benzonase® nuclease. For enzyme assays, mitochondrial fractions were resuspended in chilled Zheng buffer. Sample total protein content was determined using the BCA assay [55].

2.15. SDS-PAGE and western blotting

Protein samples were denatured by heating (70 °C, 10 min) 1.4 μg/μL sample protein together with 355 mM βME and 1× Laemmli sample buffer. Thereafter, debris was removed by centrifugation at 10000 ×*g* (5 min). Equal amounts of protein (63 μg) were separated by SDS-PAGE at 200 V on a 1.5 mm, 12 % TGX Stain-Free™ gel. Proteins were then electroblotted onto a 0.2 μm PVDF membrane at 1.3 A for 10 min. The membrane was then blocked in 1× tris buffered saline (TBS) with 1 % (*w*/*v*) casein at 22 °C for 1 h. Thereafter, the membrane was cut into two segments to separately probe for target proteins. After each subsequent incubation step, membrane segments were washed five times in 1× TBS with 0.001 % Tween®20 followed by a final wash in 1× TBS. Each membrane segment was incubated overnight at 4 °C with the primary antibody (1:100 dilution for Anti-NDUFS4 and 1:3000 dilution for Anti-VDAC1) corresponding to the specific target protein. Afterwards, membrane segments were incubated at 22 °C for 1 h with distinct horseradish peroxidase-conjugated secondary antibodies (1:10000 dilutions). Antibodies listed in Table S1. Finally, membrane segments were incubated in AEC peroxidase substrate solution (22 °C, 15 min) to initiate signal development. Protein visualization and semi-quantification were performed using the Bio-Rad ChemiDoc™ MP imaging system and Image Lab software (version 5.2.1), with NDUFS4 expression levels normalized to the mitochondrial loading control, VDAC1.

2.16. Respiratory chain enzyme assays

Kinetic spectrophotometric assays for CI-IV of the respiratory chain, as well as citrate synthase (EC 2.3.3.1) were performed according to standardized protocols based on previous reports [56–62]. Mitochondrial fractions were subjected to three freeze-thaw cycles in liquid nitrogen and cold water to ensure disruption of mitochondrial membranes and release of respiratory chain enzymes prior to analysis. Assays were performed independently in 96-well UV microtiter plates at 37 °C with triplicate reactions analyzed for each sample using the Synergy™ HT Multi-detection microplate reader (Biotek Instruments). Maximal enzyme activities were normalized to units of citrate synthase (UCS in μmol/min/mg protein) as an indicator of mitochondrial mass.

2.17. Multiplatform metabolic profiling

Metabolic profiles were obtained using a multiplatform approach comprising of untargeted proton nuclear magnetic resonance (^{1}H NMR) spectroscopy, semi-targeted liquid chromatography-tandem mass spectrometry (LC-MS/MS), untargeted gas chromatography time-of-flight mass spectrometry (GC-TOFMS), and targeted gas chromatography-tandem mass spectrometry (GC–MS/MS). Analyses were performed as previously reported [63] with modifications. Detailed descriptions of sample preparation and analysis are given in Appendix A. Supplementary data.

2.18. Metabolite extract preparation for metabolic profiling

Five replicate samples per genotype (*i.e.* distinct cultures in parallel) were prepared for each metabolic analysis. Each cell pellet, harvested from a T25 culture flasks, was washed three times with chilled PBS before being quenched in cold HPLC-grade methanol, with subsequent addition of an internal standard mixture in cold HPLC-grade water. Thereafter, samples were homogenized using a vibration mill (30 Hz, 1 min) and incubated on ice (10 min) after the addition of cold HPLC-grade chloroform. Solvents were added in a ratio of 3:1:1, methanol/water/chloroform, as required for a modified monophasic Bligh-Dyer extraction [64,65]. After centrifugation at 12000 ×*g* (10 min, 4 °C) supernatants were aliquoted into 2 mL glass vials. Intracellular extracts from a single T25 flask (~1 mL) were divided between two platforms, *i.e.*, either ^{1}H NMR spectroscopy (360 μL) and LC-MS/MS (180 μL) or GC-TOFMS (360 μL) and GC–MS/MS (360 μL). Any remaining sample volumes were pooled for a quality control (QC) sample. Next, a stable isotope mixture was added to sample aliquots intended for LC-MS/MS, all samples were dried under nitrogen, and stored at −80 °C. Prior to analysis, samples were prepared for each platform as follows. For ^{1}H NMR spectroscopy, extracts were resuspended in HPLC-grade water, centrifuged, and the supernatant mixed with TSP-d4 NMR buffer solution (90:10, *v*/v). For LC-MS/MS, extracts were butylated with 1-butanol:acetyl chloride (4:1, v/v), dried, and reconstituted in water: acetonitrile (50:50, v/v) containing 0.1 % formic acid. For GC–MS/MS, samples were resuspended in pyridine and silylated with MSTFA containing 1 % tBDMS. For GC-TOFMS, samples were oximated with methoxyamine hydrochloride in pyridine (20 mg/mL) and silylated with BSTFA containing 1 % TMCS.

2.19. Metabolic data processing

Spectral data gathered from each platform underwent automated baseline correction, peak alignment, and extraction into matrices using the relevant instrument software. Spectra were then manually reviewed to ensure correct peak picking and adequate spectral quality. Next, individual data matrices were preprocessed in Excel (Microsoft 365). This included the removal of unreliably detected variables through data filtering and the reduction of non-biological variation through normalization. A limit of detection (LOD) filter was applied to MS/MS datasets, which removed any feature areas below the assumed LOD for each platform. Thereafter, a missing value filter was applied, which only kept features in the dataset that were detected in all samples. Spectral features were then normalized to each sample's total useful signal (TUS), which is the summation of peak intensities from features that were shared in all samples [66]. To account for possible variations in ionization and ion suppression effects, metabolites detected *via* LC-MS/MS were additionally normalized to stable isotopes — either the stable-isotope of the metabolite (if available) or an isotope with a similar retention time to which the metabolite showed strong positive correlation [67]. For this purpose, Pearson's correlations were performed in MetaboAnalyst (Xia Lab, version 5.0 [68,69]). Subsequently, unreliably detected features were filtered out of datasets, as indicated by QC-CV values >25 % for targeted data or 50 % for untargeted data; and noisy features with a Fisher ratio of <0.05 [70].

2.20. Statistical analyses

Differences between groups were measured on a practical and statistical level. Effect size (Cohen's d-value ≥1) calculations were done in Excel as a measure of the practical magnitude of alterations [71]; whereas two-tailed *t*-tests were performed to measure statistical significance ($p \leq 0.05$). For metabolic data, datasets were log transformed prior to statistical analysis and *p*-values were false discovery rate (FDR)-corrected using the Bonferroni-Holm method in MetaboAnalyst to compensate for multiple testing. Metabolic data was additionally analyzed on a multivariate level in MetaboAnalyst through the application of principal component analysis (PCA) and hierarchical clustering analysis. For the latter, the Euclidean distance measure in combination with the ward linkage clustering method was used. Both multivariate approaches were used to visualize data clustering and assess whether a natural distinction was evident between KO and WT groups. These analyses were performed on a merged dataset, *i.e.*, data that originated from the same sample, but different platforms, were merged into a single data matrix. PCAs were done on all detected features as well as only significantly altered features ($p > 0.05$; d > 1); whereas hierarchical clustering heatmaps were performed only on identified metabolites. Data were log transformed and auto scaled prior to these statistical analyses.

3. Results

3.1. CRISPR-Cas9 mediates the knockout of NDUFS4 in iPSCs to generate a model of CI deficiency

iPSCs were generated from a fibroblast line of African origin with no reported disease. Briefly, an iPSC colony derived from this line with correct morphology (defined borders, containing cells with a high nucleus-cytoplasm ratio) (Fig. S1a) and with detectable expression of pluripotency markers were confirmed, post reprogramming (Fig. S1b). No residual expression of exogenous genes (Oct4, Sox2, and Klf4) were detected in the reprogrammed iPSCs (Fig. S1c). No copy number variants were observed in iPSCs (Fig. S1d). The three germ layers were differentiated from iPSCs, as detected by the expression of lineage-specific markers corresponding to the derived cell types (Fig. S1e). The correct karyotype, 46 XX was detected in iPSCs (Fig. S1f). Lastly, pluripotency markers were confirmed, post reprogramming (Fig. S1g).

To investigate CI dysfunction, iPSCs were engineered to ablate NDUFS4 for the examination of associated biochemical and metabolomic alterations. A single gRNA 1.3, shown in Fig. 1b, directed the CRISPR-Cas9 system to mediate a DSB within the first exon of the gene and incorporate indels within the *NDUFS4* coding region. The *NDUFS4* KO iPSC lines were expanded from a genome engineered population (Fig. S2a) and distinguished from the potential unedited isogenic control, WT iPSC lines by the incorporation of indels at the DSB site (Fig. S2 b). The sequencing results revealed that the WT sequence lacked indels and was homologous to the WT *NDUFS4* gene sequence. Conversely, heterozygous biallelic deletions were identified at the DSB site of the KO sequence (Fig. 1b). This biallelic modification subsequently caused a frameshift mutation leading to a premature stop codon within the coding region of the gene. The isogenic background ensures genetic uniformity, enabling precise phenotypic comparison of the impact of NDUFS4 absence (Fig. 1c) irrespective of potential variability caused by the interplay of nucleo-mitochondrial interactions associated with mitochondrial dysfunction [72]. Tabulated in Fig. 1d, is the resultant amino acid sequence of the KO with the formation of a truncated protein and, hence, an altered MTS. Tertiary structures of the truncated biallelic KO were generated using the I-TASSER online server, which constructs three-dimensional (3D) protein models using deposited protein data [73]. The predicted structures (Fig. 1d) for the KO share no homology to the native NDUFS4 structure (PDB: 5XTB) [74].

3.2. An NDUFS4 KO results in loss of NDUFS4 protein expression and reduced CI activity in iPSCs

The relative NDUFS4 protein expression was evaluated in KO and WT iPSCs ($n = 3$ replicates per group) *via* semi-quantitative western blot analysis. Western blotting data (Fig. 2a) confirmed the absence of visible NDUFS4 (18 kDa) expression in KO iPSCs, while NDUFS4 was clearly detected in the isogenic control cells. Band intensities of the protein loading control, VDAC1 (30 kDa), were similar for all samples, thereby indicating even protein loading and transfer across the lanes. Densitometric semi-quantification (Fig. 2b) further confirmed the absence of VDAC1-normalized NDUFS4 expression in the KO cells, when compared to WTs ($p < 0.001$ Cohen's d = 19.27). Thus, the biallelic frameshift deletions in the coding region of *NDUFS4* translate to protein level, resulting in the absence of mature NDUFS4 protein in KO iPSCs. Subsequently, the effect of the *NDUFS4* KO on the activity of RC enzymes, CI (EC 1.6.5.3), CII (EC 1.3.5.1), CIII (EC 1.10.2.2), and CIV (EC 1.9.3.1) were spectrophotometrically measured in iPSCs ($n = 3$ replicates per group). Results (Fig. 2c) confirm a significant (~56 %) reduction in rotenone-sensitive CI activity in KO compared to WT iPSCs ($p = 0.003$, Cohen's d = 4.05). Additionally, the *NDUFS4* KO also resulted in decreased CII (~24 %) and CIV (~29 %) activity, although these alterations were not statistically significant.

3.3. An NDUFS4 KO significantly alters iPSC metabolism

To investigate whether the *NDUFS4* KO alters the metabolic profile of iPSCs, multiplatform metabolomics was performed on KO and WT cells ($n = 5$ replicates per group). Data obtained from the same sample were combined into a single matrix as aliquots from the same sample underwent both ^{1}H NMR spectroscopy and LC-MS/MS analyses (Fig. 3a, c, and e), while separate sample aliquots underwent GC-TOFMS and GC–MS/MS analyses (Fig. 3b, d, and f). Principal component analyses (PCA, Fig. 3a-b) and hierarchical clustering analyses (Fig. 3 c-d) both confirmed distinct metabolic profiles between KO and WT iPSCs, with samples clustering together according to genotype. For both datasets, clear natural separation between genotypes was apparent upon inclusion of all detected features in the PCAs (PC1: 37.4–37.9 %), indicating prominent changes in the metabolic profiles of *NDUFS4* KO iPSCs. This distinction became even more pronounced when only significantly

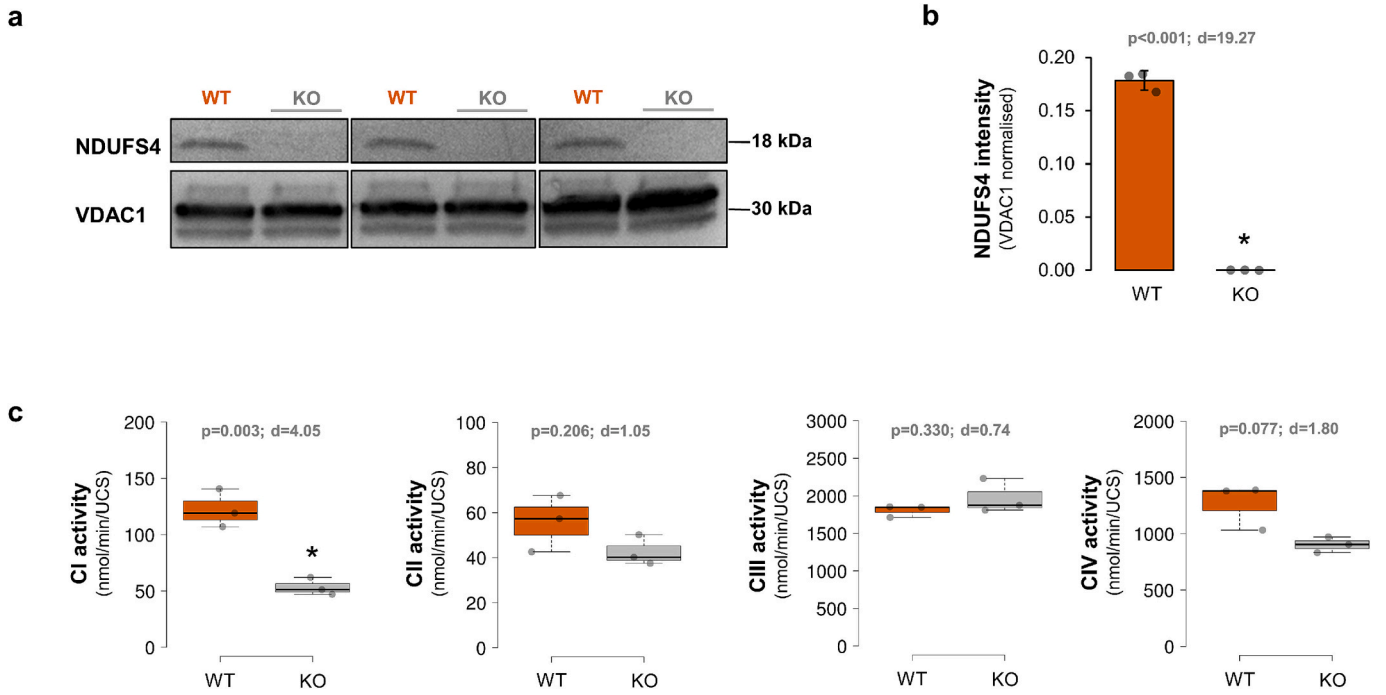

Fig. 2. NDUFS4 expression and respiratory chain enzyme activity in iPSC lines. (a) Western blot of NDUFS4 (target) and VDAC1 (loading control) in WT and KO iPSC lines. (b) Densitometric semi-quantification of NDUFS4, normalized with VDAC1. Data displayed as average ± standard deviation. Individual data points shown as dots ($n = 3$ per group). (c) Respiratory chain enzyme activity in WT and KO iPSC lines, normalized to units of citrate synthase (UCS) as quantitative mitochondrial marker. Box plots display minimum and maximum values, the inter-quartile range (box height), and median (thick horizontal line) for each group. Individual data points shown as dots (n = 3 per group) represent the mean of three technical repeats. Asterisk indicates significance, determined by two-tailed *t*-test ($p < 0.05$) and effect size calculations (Cohen's D > 1). *Abbreviations: CI, complex I; CII, complex II; CIII, complex III; complex IV; KO, knockout; iPSC, human induced pluripotent stem cell; UCS, units of citrate synthase; WT, wildtype.*

altered features ($p > 0.05$; d > 1) were included in the PCAs (PC1: 63.9–65.5 %). Hierarchical clustering heatmaps display 40 of the metabolites with the lowest *p*-values in each dataset, highlighting metabolite clusters with synchronized changes in relative abundance due to the *NDUFS4* KO. Volcano plots (Fig. 3e-f) further show the magnitude of change (Cohen's d x 10^3) and statistical significance ($-\log_{10}$[FDR-p]) of these metabolic alterations in *NDUFS4* KO iPSCs compared to WTs. Key alterations include decreased *N*-acetylasparate, *N*-acetylglutamate, kynurenine, 2-aminoadipate, pipecolate, putrescine, and aspartate along with increased trimethylglycine, glutamine, leucine, ornithine, alanine, 2-hydroxy-3-methylvalerate, myoinositol, 5′-methylthioadenosine, adenine, and threonine.

Overall, *NDUFS4* KO iPSCs displayed marked alterations in several NAD^+-dependent pathways, including glycolysis and the TCA cycle (Fig. 4a), as well as branched-chain amino acid (BCAA) catabolism (Fig. 4b). The *NDUFS4* KO resulted in decreased intracellular levels of TCA cycle metabolites, citrate, 2-ketoglutarate, and its derivative, 2-hydroxyglutarate, succinate, malate, and fumarate. *NDUFS4* KO iPSCs further exhibited significantly elevated levels of alanine, myoinositol, ketone bodies, acetoacetate and 3-hydroxybutyrate, and BCAAs. Elevated metabolite ratios (Fig. 4c), indicative of redox imbalance, were also observed.

Finally, β-lapachone (βL), a known NAD^+ modulating agent, was used to alleviate reductive stress in the *NDUFS4* KO iPSCs. Treating the KO cells with 0.05 μM βL for 24 h significantly altered the ratio of metabolites known to indicate the cytosolic (lactate/pyruvate ratio) and the mitochondrial (3-hydroxybutyrate/acetoacetate ratio) redox state, as illustrate in Fig. 4d.

4. Discussion

4.1. Generation of an iPSC model of CI deficiency caused by the knockout of NDUFS4 mediated by CRISPR-Cas9

The lack of effective therapies for mitochondrial CI deficiency is partly due to a dearth of human-relevant disease models [40,75,76]. However, within the last five years the combined technologies of iPSCs and CRISPR-Cas9 has propelled the development of robust human *in vitro* models of CI dysfunction with defective NDUFS4. These models have provided insight into potential pathomechanisms and a platform for intervention strategies. Previous studies have primarily focused on differentiating patient-derived iPSCs to investigate defects in high-energy-demanding cell types, such as neurons, where CI dysfunction manifests with definitive cellular phenotypes [39–41,77,78]. In this study, we generated isogenic *NDUFS4* KO iPSC from healthy cells to evaluate their utility in providing a relevant metabolic environment for early-stage, high-throughput exploration of therapeutic strategies for mitochondrial dysfunction.

The iPSC line genome engineered in this study possesses a genetic background that is more diverse than the available reference genome sequences (*e.g.* GRCh38), which primarily represent that of the European population. This dearth of representation poses challenges for genome editing interventions in African-ancestry populations [79–82]. Existing computational algorithms for CRISPR-gRNA design, including primer design for the screening of gene edited clones, rely on these reference genomes. Two gRNA sequences predicted to mediate optimal (>60 %) gRNA efficiencies [83] at the *NDUFS4* locus using the available reference sequence mediated 20–60-fold lowered efficiencies in this more genetically diverse iPSC line, as measured by the T7E1 mismatch cleavage assay (results not shown). The variant, rs2279516 G > C, located within *NDUFS4* exists in 78 % of the African population and

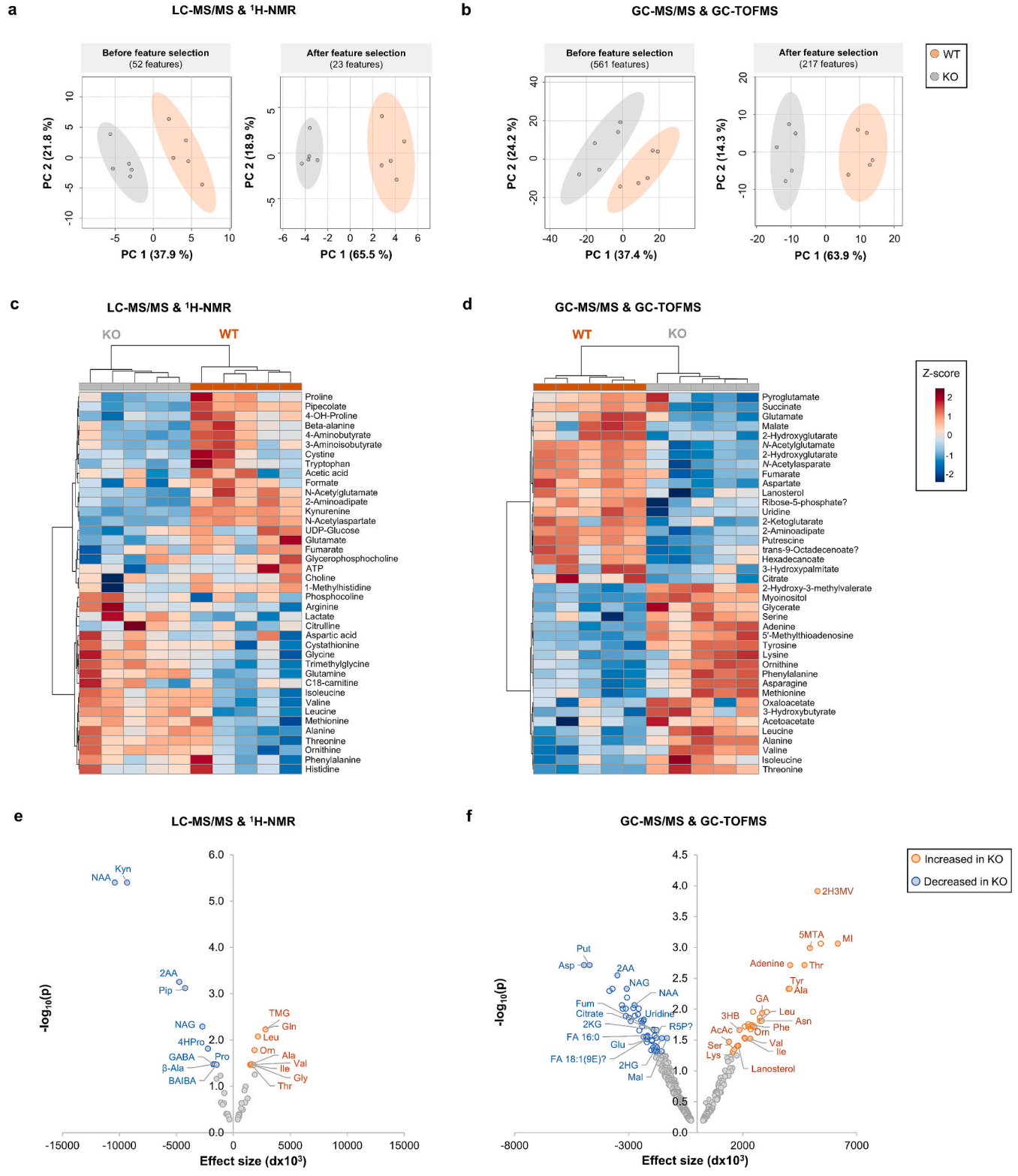

(caption on next page)

Fig. 3. Multiplatform metabolomics analysis of iPSC lines. Principal component analysis (PCA) of metabolites detected in WT and KO iPSCs *via* (a) LC-MS/MS and ^{1}H NMR spectroscopy and (b) GC–MS/MS and GC-TOFMS before and after feature selection. The scores plots display the first two principal components along with 95 % confidence intervals of groups. Data were log transformed and auto scaled ($n = 5$ per group). Hierarchical clustering heatmap of metabolite levels in iPSC lines detected *via* (c) LC-MS/MS and ^{1}H NMR spectroscopy and (d) GC–MS/MS and GC-TOFMS. Clustering was performed using the Euclidean distance measure and the ward linkage clustering method for the 40 metabolites with the lowest *t*-test *p*-value. For untargeted GC data, unknowns, and features with <80 % matches to spectral library hits, were excluded from heatmaps. Volcano plots depicting the significance *vs* effect size of metabolic alterations in iPSCs for (e) LC-MS/MS and ^{1}H NMR spectroscopy and (f) GC–MS/MS and GC-TOFMS datasets. Blue and orange filled circles respectively indicate metabolites significantly lower or higher in KO cells compared to WTs (FDR-corrected $p < 0.5$ and $d \geq 1$). Insignificant features are shown in grey. For untargeted GC data, unknowns were excluded and features with <80 % matches to spectral library hits are indicated with empty circles. Question marks next to metabolite names indicate a lower identification confidence level *i.e.*, metabolites for which the identity should be confirmed. Statistical significance (y-axis) depicted as negative logarithm to the base 10 ($-\log_{10}$) of FDR-corrected *p*-values. Effect sizes (x-axis), calculated using Cohen's d (d x 10^{3}). *Abbreviations: 2AA, 2-aminoadipate; 2H3MV, 2-hydroxy-3-methylvalerate; 2HG, 2-hydroxyglutarate; 2KG, 2-ketoglutarate; 3HB, 3-hydroxybutyrate; 4HPro, 4-hydroxyproline; 5MTA, 5′-methylthioadenosine; AcAc, acetoacetate; Ala, alanine; Asn, asparagine; Asp, aspartate; BAIBA, 3-aminoisobutyrate; FA 16:0, hexadecanoate [palmitate]; FA 18:1(9E)?, trans-9-octadecenoate [elaidic acid]?; Fum, fumarate; GA, glycerate; GABA, 4-aminobutyrate; Gln, glutamine; Glu, glutamate; Gly, glycine; Ile, isoleucine; Kyn, kynurenine; Leu, leucine; Lys, lysine; Mal, malate; MI, myoinositol; NAA, N-acetylaspartate; NAG, N-acetylglutamate; Orn, ornithine; Phe, phenylalanine; Pip, pipecolate; Pro, proline; Put, putrescine; R5P?, ribose-5-phosphate?; Ser, serine; Suc, succinate; Thr, threonine; TMG, trimethylglycine [Betaine]; Tyr, tyrosine; Val, valine; β-Ala, beta-alanine.* (For interpretation of the references to colour in this figure legend, the reader is referred to the web version of this article.)

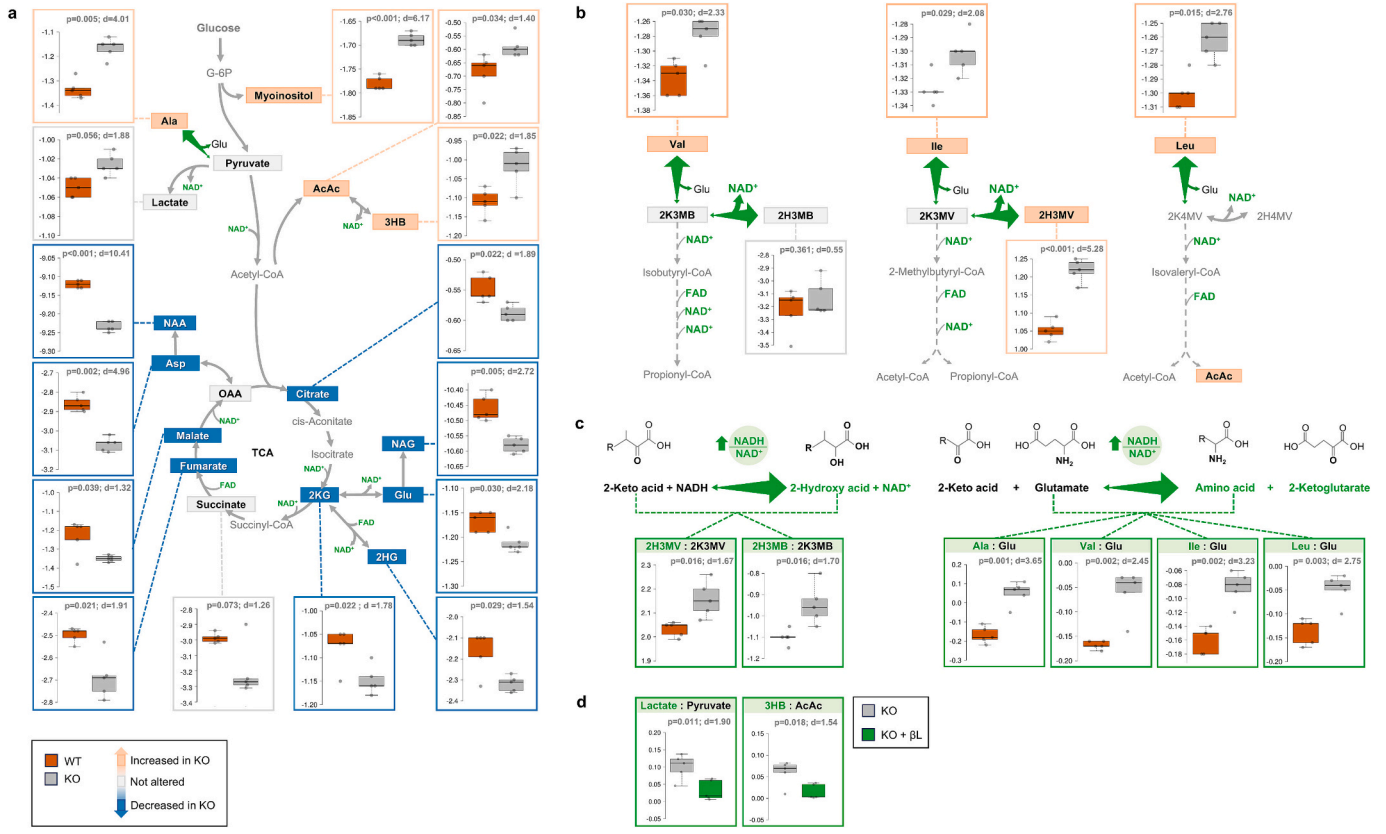

Fig. 4. Major metabolic pathways altered in *NDUFS4* KO iPSCs. Metabolic alterations observed in (a) glycolysis and the TCA cycle and (b) branched chain amino acid catabolism. Box plots depict the relative intensity of metabolites significantly altered in KO (grey) compared to WT (orange) iPSCs. (c) Metabolic indicators of NADH/NAD^{+} ratio. An increased NADH/NAD^{+} ratio drives the formation of 2-hydroxy acids and NAD^{+} (from 2-keto acids and NADH) as well as amino acids (from 2-ketoacids and glutamic acid). Significance was determined by two-tailed *t*-test, with false discovery rate (FDR) correction for multiple testing applied, and effect size calculations. FDR-corrected *p*-values and Cohen's d values are displayed on box plots. Statistically significant metabolic alterations are indicated by blue boxes, if decreased, or peach boxes, if increased, in KO iPSCs. (d) Alleviation of reductive stress in the KO iPSCs by β-lapachone (βL). The ratios of specific metabolic markers are used as indication of the redox status in the cytosol (lactate/pyruvate ratio) and mitochondria (3-hydroxybutyrate/acetoacetate ratio). Grey boxes indicate metabolites that were not significantly altered. Green arrows and boxes highlight metabolites and metabolite ratios related to redox status. *Abbreviations: 2H4MV, 2-hydroxy-4-methylvalerate; 2H3MV, 2-hydroxy-3-methylvalerate; 2HG, 2-hydroxyglutarate; 2KG, 2-ketoglutarate; 2K3MB, 2-keto-3-methylbutyrate; 2K3MV, 2-keto-3-methylvalerate; 2K4MV, 2-keto-4-methylvalerate; 3HB, 3-hydroxybutyrate; AcAc, acetoacetate; Ala, alanine; Asp, aspartate; Glu, glutamate; Ile, isoleucine; Leu, leucine; NAA, N-acetylaspartate; NAG, N-acetylglutamate; OAA, oxaloacetate; Val, valine. (For interpretation of the references to colour in this figure legend, the reader is referred to the web version of this article.)*

resides proximal to the protospacer adjacent motif of the predicted gRNAs. This SNP significantly reduced Cas9 cleavage at the *NDUFS4* locus in this iPSC line owing to the mismatches in the gRNA sequences [79,82,84] compared to a 3-fold reduction (>60 % predicted efficiency) in efficiency mediated by gRNA 1.3, without any mismatches to the *NDUFS4* locus. This underscores the importance of accounting for genetic variation in underrepresented populations to implement effective genome engineering and allow for equitable drug screening and clinical intervention [79,82,85].

4.2. An NDUFS4 KO results in loss of NDUFS4 protein expression and reduced CI activity in iPSCs

In line with studies on CI deficient patients and animal models [22,86,87], the loss of NDUFS4 in iPSCs reduced, but did not abolish, CI activity with ~44 % residual CI activity remaining. As an accessory subunit of the CI N-module, NDUFS4 plays a critical role in CI assembly, stability, and function. NDUFS4 loss decreases the levels of other CI subunits and destabilizes CI N- to Q-module attachment, resulting in the formation of N- and Q/P-module subassemblies instead of holo-CI. While these subassemblies are inactive under blue-native-PAGE conditions, a level of residual CI activity is sustained *in situ* [87]. This residual activity is crucial for maintaining viable phenotypes as complete loss of CI activity is deemed incompatible with life [22,88]. Although NDUFS4 loss, on average, results in a 50 % reduction of CI activity in patient fibroblasts [18], the degree of CI deficiency varies greatly among individuals and tissue types, with residual CI activity ranging from 15 to 75 % of control values in *NDUFS4*-mutated patient fibroblasts [18,24,86,87,89] and 9–44 % of control values in *Ndufs4* KO mouse tissues: lung (9 %), pancreas (17 %), liver (19 %), kidney (25 %), whole brain (26 %) [22], olfactory bulbs (14 %), brainstem (25 %), cerebellum (28 %) and anterior cortex (38 %) [90], skeletal muscles (20–29 %) [22,91], and heart (44 %) [22].

NDUFS4 KO iPSCs also displayed moderate reductions in CII (~24 %) and CIV (~29 %) activity. This observation aligns with the notion that primary disruptions in CI assembly can secondarily affect other respiratory chain complexes due to their organization into supercomplexes (SCs). The abundance of specific CI subunits directly influences the assembly of CI into SCs [92,93]. While NDUFS4 loss does not seem to directly affect CII-CIV expression [22,86,87], it does cause minor catalytic deficiencies (18–25 % activity loss) in CII-IV [86] and results in the loss of CI- and CIV-containing SCs in *Ndufs4* KO mice [22,39]. Although SC formation has been proposed to facilitate substrate channeling, enhance electron transport efficiency, and modulate ROS production, these roles are highly debated and much remains to be discovered about the cell type-specific bioenergetic and physiological roles of SCs [94–96]. Taken together, the extent of CI deficiency observed in our iPSC model, and its secondary, catalytic impairment of other RC enzymes aligns well with findings from other models of mitochondrial disease.

4.3. NDUFS4 KO iPSCs display a metabolic phenotype characteristic of mitochondrial disease

The metabolic perturbations detected in *NDUFS4* KO iPSCs is in keeping with the altered metabolome of mitochondrial disease described earlier, including metabolic data from the *Ndufs4* KO mouse model of CI deficiency [63,90,91,97,98], different pre-clinical mitochondrial disease models (cells, nematodes, and mice), and patient samples (urine, plasma, and skeletal muscle) [99], together with patients carrying the highly prevalent m.3243A > G mtDNA mutation, which affects CI, CIII, CIV, and CV [100,101].

A hallmark consequence of an *NDUFS4* KO, is intracellular NADH/NAD^+ redox imbalance, as CI is a major contributor to NADH oxidation [102–104]. NADH/NAD^+ balance and NAD^+ availability, is tightly linked to the regulation of numerous metabolic pathways, which are known to be perturbed in mitochondrial disease models and patients [41,63,97,99,100,102,105–107]. The metabolic perturbations detected in the *NDUFS4* KO iPSCs also align well with previous work on mitochondrial disease tissue cultures [97,108], where the iPSCs display metabolic alterations in the TCA cycle, including (i) alanine accumulation, indicative of diminished pyruvate oxidation; (ii) decreased levels of TCA cycle intermediates (citrate, 2-ketoglutarate, succinate, malate, and fumarate), suggesting decreased oxidative TCA cycling; (iii) increased levels of glutamine along with decreased levels of glutamate, aspartate, and their acetylated derivatives, suggesting altered glutamine handling within the TCA cycle and (iv) elevations in ketone bodies (acetoacetate and 3-hydroxybutyrate), which reflect alterations in acetyl-CoA levels and/or fatty acid oxidation. Furthermore, alanine accumulation is one of the most consistent findings across various mitochondrial disease models and patient samples [99], including m.3243A > G patient urine [101], *Ndufs4* KO mouse urine, brain regions [63], and whole brain mitochondrial and cytosolic fractions [98]. In our results, alanine is also strongly increased in the KO iPSCs, compared to the WT iPSCs.

Interestingly, decreased *N*-acetylaspartate (NAA) was one of the most significant alterations observed in *NDUFS4* KO iPSCs. Initially considered exclusive to the brain, the physiological role of NAA remains debated but seems to extend beyond the central nervous system [109]. NAA is synthesized from aspartate and acetyl-CoA, with its enzymatic cleavage generating aspartate and acetate. We previously reported perturbed NAA levels in *Ndufs4* KO mice, which increased in skeletal muscles and decreased in the olfactory bulbs — one of the first and most affected brain regions in this mouse model [63]. Lower NAA levels may indicate compromised mitochondrial function, as NAA is synthesized in the mitochondrion and therefore reflects the organelle's metabolic activity. Consequently, lower NAA levels can serve as a marker of mitochondrial dysfunction, altered TCA cycle activity, and potential metabolic disturbances [110]. The substantially lower levels of NAA detected in the KO iPSCs, therefore, indicate markedly reduced TCA cycle activity and reduced energy production *via* oxidative phosphorylation. The known cellular consequences of this stalled TCA cycle are immense, including altered fatty acid and amino acid metabolism causing a disruption of anaplerotic reactions, increase reliance on glycolysis for ATP production, elevated oxidative stress and eventually apoptosis [97,111,112].

Perturbations in the NAD^+-dependent pathways of BCAA catabolism is another strong metabolic signature associated with mitochondrial disease-related redox imbalance [99]. As seen in *NDUFS4* KO iPSCs, BCAA levels and BCAA:glutamate ratios were significantly elevated in the blood of a heterogenous group of primary respiratory chain disease patients [113] as well as brain regions [90] and whole brain mitochondrial fractions [98] from *Ndufs4* KO mice. Similar findings were also reported for CI, CII, and CIII KO nematode models [114], the deletor mouse model with multiple mtDNA deletions, and patients with mtDNA replication disorders [115]. During the second step in BCAA catabolism, the NAD^+-dependent branched-chain alpha-keto acid dehydrogenase enzyme complex converts branched-chain keto acids (BCKAs) to their CoA esters. The inhibition of this step due to NADH accumulation may prompt BCKAs to revert to their corresponding BCAAs or be reduced to branched-chain hydroxy acids (BCHAs), producing NAD^+ in an effort to maintain homeostasis [116,117]. Thus, the significant increase in BCAA levels, BCAA:glutamate ratios, and BCHA:BCKA ratios detected in *NDUFS4* KO iPSCs, are indicative of an increased NADH/NAD^+ ratio that drives the formation of amino acids, from 2-keto acids and glutamate [113] as well as 2-hydroxy acids and NAD^+ from 2-keto acids and NADH [118–122].

β-Lapachone (βL), a known NAD^+ modulator, was used to alleviate reductive stress in *NDUFS4* KO cells. βL accelerates the NAD(*P*)H: quinone oxidoreductase-dependent oxidation of NADH to NAD^+ both *in vitro* and *in vivo* by receiving two electrons from NADH [123]. Treatment of *NDUFS4* KO iPSCs with 0.05 μm βL, significantly altered the ratio of specific metabolites known to indicate cellular redox state. While the lactate/pyruvate ratio provides information on the cytosolic redox state of the cell, the 3-hydroxybutyrate/acetoacetate ratio reflects the mitochondrial redox state [124]. Thus, βL treatment significantly reduced reductive stress, a hallmark of mitochondrial dysfunction [102–104], in *NDUFS4* KO iPSCs. However, in order to determine if βL can fully restore the metabolic profile of the *NDUFS4* KO iPSCs, a comprehensive metabolic profile should be obtained. Furthermore, isogenic controls should also be treated with βL to determine the effect of the treatment in controls.

iPSCs in their pluripotent state offer a unique platform for early-stage

drug screening, as demonstrated here by the mitigation of reductive stress in *NDUFS4* KO iPSCs using βL. By acting as a modulator of NAD^+ metabolism, βL was previously shown to prevent age-dependent decline of motor and cognitive function in aged mice [125] and was also used as an NAD^+ booster to prevent mitochondrial toxicity in tissue cultures treated with cisplatin, a first-line chemotherapeutic drug [126]. This amelioration of reductive stress in *NDUFS4* KO cells using βL has, to the best of our knowledge, never been reported before in a mitochondrial disease tissue culture model.

Altogether, our *NDUFS4* KO iPSC model exhibits a metabolic profile in line with preclinical models of, and patients with, mitochondrial disease — highlighting the central role of NADH/NAD^+ redox balance in cellular metabolism. Although iPSCs primarily rely on glycolysis and glutamine metabolism, their metabolic phenotype is flexible [127]. IPSCs have fully operational respiratory chain complexes [128] and adapt their metabolism based on nutrient availability/media composition, maintaining self-renewal capacity while utilizing either glycolytic or oxidative mitochondrial pathways [127]. Hence, the strong metabolic phenotype seen in *NDUFS4* KO iPSCs, reinforces the idea that mitochondrial function and oxidative metabolism are neither contradictory to nor expendable for iPSCs in the pluripotent state, contrary to common belief [127].

4.4. Future applications

The strong metabolic phenotype observed in *NDUFS4* KO iPSCs suggests that this model can be used as a drug screening tool in the undifferentiated, pluripotent state. By circumventing the requirement for laborious differentiation protocols [129], iPSCs offer distinct advantages for drug screening assays in terms of time and cost efficiency. In line with this, Platani, et al. [42] showed that screening different iPSC lines in their pluripotent state reveals variable drug responses relevant to the genetic background of the donor. Additionally, the pronounced impact that the loss of NDUFS4 has on the redox status in iPSCs, underscores the suitability of NADH/NAD^+ balance, or metabolic indicators thereof, as a robust marker for inclusion in drug screening assays. Instead of conducting extensive metabolic analyses, a single assessment focusing on a few key redox markers could suffice, like measuring the ratio of one or two BCAAs to glutamate or even the ratio of BCHAs to BCKAs. Alternatively, immunofluorescent microscopy utilizing a redox probe presents a viable approach with which to monitor treatment efficacy. Another way to evaluate the effectiveness of treatment options is to quantify NAA, the metabolite most significantly reduced in *NDUFS4* KO iPSCs, both in terms of *p*-value and effect size. Normalization, or partial normalization of this metabolite during treatment, relative to the WT iPSCs, would indicate a metabolic rescue of the *NDUFS4* KO iPSCs.

Considering the tissue-specific vulnerability seen in mitochondrial diseases, the development of genetically modified iPSC models is essential for unravelling disease mechanisms across different cell and tissue types [130]. The capability to differentiate *NDUFS4* KO iPSCs into diverse cell types such as brain, heart, liver, and muscle, is advantageous. Moreover, producing 3D organoids that better reflect the *in vivo* microenvironment of specific tissues offers further benefit. Unlike 2D cultures, 3D culture-systems better represent the *in vivo* extracellular matrix (ECM) microenvironment, cell-to-ECM interactions, cell-to-cell interactions from multiple directions, and mechanical cues from cellular stretch [131–133]. Since neurotoxicity and neuroinflammation was reported as a hallmark of CI deficiency in the *Ndufs4* KO mouse model [134,135], a model involving crosstalk between iPSC-derived neurons or neural organoids and microglia may provide the required phenotypic complexity to investigate the mechanism of CI dysfunction [136]. This approach can aid in comprehensively characterizing CI deficiency by providing insights into the mechanisms underlying tissue-specific phenotypic manifestations within the same genetic background.

Therefore, the model developed here holds promise to be used as a drug screening tool in the pluripotent state or it can be differentiated to different cell types to study the mechanisms involved in the tissue specificity commonly encountered in mitochondrial disease.

5. Conclusion

This study details the development of an *NDUFS4* KO iPSC model derived from an individual of African descent. To our knowledge, this is the first comprehensive measurement of CI-CIV respiratory chain enzyme activity and metabolic alterations in *NDUFS4* KO iPSCs at the pluripotent level. The genome editing strategy employed to generate isogenic iPSCs allowed the dissection of subtle metabolic differences attributed to the loss of NDUFS4. *NDUFS4* KO iPSCs exhibit a clear metabolic phenotype that aligns well with established metabolic signatures of mitochondrial dysfunction. Subsequent treatment of *NDUFS4* KO iPSCs with a potent NAD^+ modulator, βL, significantly alleviated reductive stress — confirming the applicability of this model as a possible first-level drug screening platform for mitochondrial dysfunction.

Ethical approval

Procedures performed at the CSIR were in accordance with the approved protocol, Development of a cellular model of infectious disease investigating drug toxicity, with ethical clearance number REF: 77/2013. Subsequent procedures performed at the NWU were approved by the NWU Health Research Ethics Committee (NWU-HREC, approval number NWU-00228-22-A1).

CRediT authorship contribution statement

Shivani Goolab: Writing – original draft, Visualization, Methodology, Investigation, Formal analysis, Conceptualization. **Karin Terburgh:** Writing – original draft, Visualization, Formal analysis, Conceptualization. **Charl du Plessis:** Writing – review & editing, Methodology, Investigation, Formal analysis, Conceptualization. **Janine Scholefield:** Writing – review & editing, Resources, Conceptualization. **Roan Louw:** Writing – review & editing, Supervision, Resources, Investigation, Funding acquisition, Conceptualization.

Declaration of competing interest

The authors declare that they have no known competing financial interests or personal relationships that could have influenced the work reported in this paper.

Acknowledgements

Funding: This work was supported by the National Research Foundation of South Africa (NRF Grant no 120829), the North-West University (NWU), and by the Parliamentary grant funding of South Africa, Council for Scientific and Industrial Research (CSIR). Opinions expressed and conclusions arrived at are those of the authors and are not necessarily to be attributed to the NRF, NWU, or CSIR. We would also like to thank Jana Theron, Hanné Haasbroek, and Ashley Judkins for their assistance with some of the experimental work.

Appendix A. Supplementary data

Supplementary data to this article can be found online at https://doi.org/10.1016/j.bbadis.2024.167569.

Data availability

The data from this study are available through the NIH Common Fund's Data Repository and Coordinating Center, supported by NIH

grant U01-DK097430, at the Metabolomics Workbench website (http://www. metabolomicsworkbench.org), ID: ST003544.

References

[1] S. Rahman, Mitochondrial disease in children, J. Intern. Med. 287 (2020) 609–633.
[2] Y.S. Ng, et al., Mitochondrial disease in adults: recent advances and future promise, Lancet Neurol. 20 (2021) 573–584.
[3] O.M. Russell, et al., Mitochondrial diseases: Hope for the future, Cell 181 (2020) 168–188.
[4] G.T. Rezin, et al., Mitochondrial dysfunction and psychiatric disorders, Neurochem. Res. 34 (2009) 1021–1029.
[5] D.J. van Rensburg, et al., Ndufs4 KO mice: a model to study comorbid mood disorders associated with mitochondrial dysfunction, Pharmacol. Biochem. Behav. 234 (2024) 173689.
[6] S.E. Kruse, et al., Mice with mitochondrial complex I deficiency develop a fatal encephalomyopathy, Cell Metab. 7 (2008) 312–320.
[7] W.-S. Choi, et al., Conditional deletion of Ndufs4 in dopaminergic neurons promotes Parkinson's disease-like non-motor symptoms without loss of dopamine neurons, Sci. Rep. 7 (2017) 44989.
[8] H. Gao, et al., Ndufs4 knockout induces transcriptomic signatures of Alzheimer's Diseases that are partially reversed by mitochondrial complex I inhibitor, bioRxiv (2024), https://doi.org/10.1101/2024.02.20.581247 [Preprint].
[9] K. Mise, et al., NDUFS4 regulates cristae remodeling in diabetic kidney disease, Nat. Commun. 15 (2024) 1965.
[10] J.M. Berthiaume, et al., Mitochondrial NAD+/NADH redox state and diabetic cardiomyopathy, Antioxid. Redox Signal. 30 (2017) 375–398.
[11] D.M. Kirby, et al., Respiratory chain complex I deficiency: an underdiagnosed energy generation disorder, Neurology 52 (1999) 1255–1264.
[12] D. Ghezzi, M. Zeviani, Human diseases associated with defects in assembly of OXPHOS complexes, Essays Biochem. 62 (2018) 271–286.
[13] C.L. Alston, et al., The genetics and pathology of mitochondrial disease, J. Pathol. 241 (2017) 236–250.
[14] J. Smeitink, et al., Human NADH:Ubiquinone Oxidoreductase, J. Bioenerg. Biomembr. 33 (2001) 259–266.
[15] S.J. Hoefs, et al., Molecular base of biochemical complex I deficiency, Mitochondrion 12 (2012) 520–532.
[16] R.P. Saneto, Mitochondrial diseases: expanding the diagnosis in the era of genetic testing, J Transl Genet Genom 4 (2020) 384–428.
[17] R.E. Lamont, et al., A novel NDUFS4 frameshift mutation causes Leigh disease in the Hutterite population, Am. J. Med. Genet. A 173 (2017) 596–600.
[18] J.D. Ortigoza-Escobar, et al., Ndufs4 related Leigh syndrome: a case report and review of the literature, Mitochondrion 28 (2016) 73–78.
[19] A. González-Quintana, et al., Uniparental isodisomy as a cause of mitochondrial complex I respiratory chain disorder due to a novel splicing NDUFS4 mutation, Mol. Genet. Metab. 131 (2020) 341–348.
[20] T. Emahazion, et al., Intron based radiation hybrid mapping of 15 complex I genes of the human electron transport chain, Cytogenet. Cell Genet. 82 (1998) 115–119.
[21] L. van den Heuvel, et al., Demonstration of a new pathogenic mutation in human complex I deficiency: a 5-bp duplication in the nuclear gene encoding the 18-kD (AQDQ) subunit, Am. J. Hum. Genet. 62 (1998) 262–268.
[22] M.A. Calvaruso, et al., Mitochondrial complex III stabilizes complex I in the absence of NDUFS4 to provide partial activity, Hum. Mol. Genet. 21 (2012) 115–120.
[23] F. Valsecchi, et al., Complex I disorders: causes, mechanisms, and development of treatment strategies at the cellular level, Dev. Disabil. Res. Rev. 16 (2010) 175–182.
[24] M.E. Breuer, et al., Cellular and animal models for mitochondrial complex I deficiency: a focus on the NDUFS4 subunit, IUBMB Life 65 (2013) 202–208.
[25] M.A.E. van de Wal, et al., Ndufs4 knockout mouse models of Leigh syndrome: pathophysiology and intervention, Brain 145 (2022) 45–63.
[26] Y. Shi, et al., Induced pluripotent stem cell technology: a decade of progress, Nat. Rev. Drug Discov. 16 (2017) 115–130.
[27] R.H. Anderson, K.R. Francis, Modeling rare diseases with induced pluripotent stem cell technology, Mol. Cell. Probes 40 (2018) 52–59.
[28] C.L. McKnight, et al., Modelling mitochondrial disease in human pluripotent stem cells: what have we learned? Int. J. Mol. Sci. 22 (2021) 7730.
[29] Y. Avior, et al., Pluripotent stem cells in disease modelling and drug discovery, Nat. Rev. Mol. Cell Biol. 17 (2016) 170–182.
[30] K. Takahashi, et al., Induction of pluripotent stem cells from fibroblast cultures, Nat. Protoc. 2 (2007) 3081–3089.
[31] F. Soldner, R. Jaenisch, Stem cells, genome editing, and the path to translational medicine, Cell 175 (2018) 615–632.
[32] M. Platani, et al., Screening for variable drug responses using human iPSC cohorts, bioRxiv (2023), https://doi.org/10.1101/2023.06.16.545161 [Preprint].
[33] M.H. Geurts, H. Clevers, CRISPR engineering in organoids for gene repair and disease modelling, Nat Rev Bioeng 1 (2023) 32–45.
[34] M. Jinek, et al., A programmable dual-RNA-guided DNA endonuclease in adaptive bacterial immunity, Science 337 (2012) 816–821.
[35] L. Cong, et al., Multiplex genome engineering using CRISPR/Cas systems, Science 339 (2013) 819–823.
[36] P. Mali, et al., RNA-guided human genome engineering via Cas9, Science 339 (2013) 823–826.
[37] M.J. Falk, The pursuit of precision mitochondrial medicine: harnessing preclinical cellular and animal models to optimize mitochondrial disease therapeutic discovery, J. Inherit. Metab. Dis. n/a (2020) 1–3.
[38] CONGRESS.GOV, S.5002- FDA Modernization Act 2.0, 2022.
[39] F. Bertan, et al., Comparative analysis of CI- and CIV-containing respiratory supercomplexes at single-cell resolution, Cell Rep Methods 1 (2021).
[40] G. Inak, et al., Defective metabolic programming impairs early neuronal morphogenesis in neural cultures and an organoid model of Leigh syndrome, Nat. Commun. 12 (2021) 1929.
[41] J.-Y. Yoon, et al., Metabolic rescue ameliorates mitochondrial encephalo-cardiomyopathy in murine and human iPSC models of Leigh syndrome, Clin. Transl. Med. 12 (2022) e954.
[42] M. Platani, et al., Screening for variable drug responses using human iPSC cohorts, bioRxiv (2023) [Preprint] doi: https://doi.org/10.1101/2023.06.16.545161.
[43] J. Yamane, et al., StemPanTox: a fast and wide-target drug assessment system for tailor-made safety evaluations using personalized iPS cells, iScience 25 (2022) 104538.
[44] G.R. Martin, Isolation of a pluripotent cell line from early mouse embryos cultured in medium conditioned by teratocarcinoma stem cells, Proc. Natl. Acad. Sci. U. S. A. 78 (1981) 7634–7638.
[45] M.J. Evans, M.H. Kaufman, Establishment in culture of pluripotential cells from mouse embryos, Nature 292 (1981) 154–156.
[46] L.F. Meisner, J.A. Johnson, Protocols for cytogenetic studies of human embryonic stem cells, Methods 45 (2008) 133–141.
[47] S.M. Hussein, et al., Copy number variation and selection during reprogramming to pluripotency, Nature 471 (2011) 58–62.
[48] M. Martí, et al., Characterization of pluripotent stem cells, Nat. Protoc. 8 (2013) 223–253.
[49] J.-P. Concordet, M. Haeussler, CRISPOR: intuitive guide selection for CRISPR/Cas9 genome editing experiments and screens, Nucleic Acids Res. 46 (2018) W242–W245.
[50] L. Vouillot, et al., Comparison of T7E1 and surveyor mismatch cleavage assays to detect mutations triggered by engineered nucleases, G3 (Bethesda) 5 (2015) 407–415.
[51] F.A. Ran, et al., Genome engineering using the CRISPR-Cas9 system, Nat. Protoc. 8 (2013) 2281–2308.
[52] C.A. Schneider, et al., NIH image to ImageJ: 25 years of image analysis, Nat. Methods 9 (2012) 671–675.
[53] B. Yang, et al., Purification, cloning, and characterization of the CEL I nuclease, Biochemistry 39 (2000) 3533–3541.
[54] C.A. Oleykowski, et al., Mutation detection using a novel plant endonuclease, Nucleic Acids Res. 26 (1998) 4597–4602.
[55] P.K. Smith, et al., Measurement of protein using bicinchoninic acid, Anal. Biochem. 150 (1985) 76–85.
[56] S. Rahman, et al., Leigh syndrome: clinical features and biochemical and DNA abnormalities, Ann. Neurol. 39 (1996) 343–351.
[57] A.J. Janssen, et al., Spectrophotometric assay for complex I of the respiratory chain in tissue samples and cultured fibroblasts, Clin. Chem. 53 (2007) 729–734.
[58] C. Luo, et al., An improved spectrophotometric method for a more specific and accurate assay of mitochondrial complex III activity, Clin. Chim. Acta 395 (2008) 38–41.
[59] R.J.T. Rodenburg, Biochemical diagnosis of mitochondrial disorders, J. Inherit. Metab. Dis. 34 (2011) 283–292.
[60] M. Spinazzi, et al., Assessment of mitochondrial respiratory chain enzymatic activities on tissues and cultured cells, Nat. Protoc. 7 (2012) 1235–1246.
[61] F.N. Gellerich, et al., The problem of interlab variation in methods for mitochondrial disease diagnosis: enzymatic measurement of respiratory chain complexes, Mitochondrion 4 (2004) 427–439.
[62] B. Errede, et al., Preparation and properties of complex IV (ferrocytochrome c: oxygen oxidoreductase EC 1.9.3.1), Methods Enzymol. 53 (1978) 40–47.
[63] K. Terburgh, et al., Cross-comparison of systemic and tissue-specific metabolomes in a mouse model of Leigh syndrome, Metabolomics 17 (2021) 101.
[64] J. Gullberg, et al., Design of experiments: an efficient strategy to identify factors influencing extraction and derivatization of Arabidopsis thaliana samples in metabolomic studies with gas chromatography/mass spectrometry, Anal. Biochem. 331 (2004) 283–295.
[65] H. Wu, et al., High-throughput tissue extraction protocol for NMR- and MS-based metabolomics, Anal. Biochem. 372 (2008) 204–212.
[66] B.M. Warrack, et al., Normalization strategies for metabonomic analysis of urine samples, J. Chromatogr. B 877 (2009) 547–552.
[67] S. Bijlsma, et al., Large-scale human metabolomics studies: a strategy for data (pre-) processing and validation, Anal. Chem. 78 (2006) 567–574.
[68] Z. Pang, et al., MetaboAnalyst 5.0: narrowing the gap between raw spectra and functional insights, Nucleic Acids Res. 49 (2021) W388–W396.
[69] J. Xia, et al., MetaboAnalyst: a web server for metabolomic data analysis and interpretation, Nucleic Acids Res. 37 (2009) W652–W660.
[70] K.M. Pierce, et al., Fisher ratio method applied to third-order separation data to identify significant chemical components of metabolite extracts, Anal. Chem. 78 (2006) 5068–5075.
[71] S. Ellis, H. Steyn, Practical significance (effect sizes) versus or in combination with statistical significance (p-values): research note, Manag. Dyn. 12 (2003) 51–53.

[72] P. Bénit, et al., Genetic background influences mitochondrial function: modeling mitochondrial disease for therapeutic development, Trends Mol. Med. 16 (2010) 210–217.
[73] Y. Zhang, I-TASSER server for protein 3D structure prediction, BMC Bioinformatics 9 (2008) 40.
[74] R. Guo, et al., Architecture of human mitochondrial respiratory megacomplex I(2)III(2)IV(2), Cell 170 (2017) 1247–1257, e1212.
[75] M. Gerards, et al., Leigh syndrome: resolving the clinical and genetic heterogeneity paves the way for treatment options, Mol. Genet. Metab. 117 (2016) 300–312.
[76] T. Galera-Monge, et al., Mitochondrial dysfunction and calcium dysregulation in Leigh syndrome induced pluripotent stem cell derived neurons, Int. J. Mol. Sci. 21 (2020).
[77] N. Daneshgar, et al., Activated microglia and neuroinflammation as a pathogenic mechanism in Leigh syndrome, Front. Neurosci. 16 (2022) 1068498.
[78] G. Sonsalla, et al., Direct neuronal reprogramming of NDUFS4 patient cells identifies the unfolded protein response as a novel general reprogramming hurdle, Neuron 112 (2024) 1117–1132, e1119.
[79] M.C. Canver, et al., Impact of genetic variation on CRISPR-Cas targeting, Crispr j 1 (2018) 159–170.
[80] S.A. Misek, et al., Germline variation contributes to false negatives in CRISPR-based experiments with varying burden across ancestries, Nat. Commun. 15 (2024) 4892.
[81] One pangenome to bind them all, Nat. Biotechnol. 40 (2022) 1301.
[82] S. Goolab, J. Scholefield, Making gene editing accessible in resource limited environments: recommendations to guide a first-time user, Front Genome Edit 6 (2024).
[83] M. Haeussler, et al., Evaluation of off-target and on-target scoring algorithms and integration into the guide RNA selection tool CRISPOR, Genome Biol. 17 (2016) 148.
[84] J.P.K. Bravo, et al., Structural basis for mismatch surveillance by CRISPR-Cas9, Nature 603 (2022) 343–347.
[85] G. Sirugo, et al., The missing diversity in human genetic studies, Cell 177 (2019) 26–31.
[86] F. Valsecchi, et al., Metabolic consequences of NDUFS4 gene deletion in immortalized mouse embryonic fibroblasts, Biochim Biophys Acta Bioenerg 2012 (1817) 1925–1936.
[87] M.J.W. Adjobo-Hermans, et al., NDUFS4 deletion triggers loss of NDUFA12 in Ndufs4−/− mice and Leigh syndrome patients: a stabilizing role for NDUFAF2, Biochim. Biophys. Acta Bioenerg. 1861 (2020) 148213.
[88] J.D. Meisel, et al., Hypoxia and intra-complex genetic suppressors rescue complex I mutants by a shared mechanism, Cell 187 (2024) 659–675, e618.
[89] S. Koene, et al., Natural disease course and genotype-phenotype correlations in complex I deficiency caused by nuclear gene defects: what we learned from 130 cases, J. Inherit. Metab. Dis. 35 (2012) 737–747.
[90] K. Terburgh, et al., Aberrant BCAA and glutamate metabolism linked to regional neurodegeneration in a mouse model of Leigh syndrome, Biochim. Biophys. Acta Mol. basis Dis. 1867 (2021) 166082.
[91] K. Terburgh, et al., Metabolomics of Ndufs4−/− skeletal muscle: adaptive mechanisms converge at the ubiquinone-cycle, Biochim Biophys Acta Mol Basis Dis 2019 (1865) 98–106.
[92] T. Arroum, et al., Loss of respiratory complex I subunit NDUFB10 affects complex I assembly and supercomplex formation, Biol. Chem. 404 (2023) 399–415.
[93] I. Lopez-Fabuel, et al., Complex I assembly into supercomplexes determines differential mitochondrial ROS production in neurons and astrocytes, Proc. Natl. Acad. Sci. U. S. A. 113 (2016) 13063–13068.
[94] A. Kohler, et al., The functional significance of mitochondrial respiratory chain supercomplexes, EMBO Rep. 24 (2023) e57092.
[95] D. Milenkovic, et al., Preserved respiratory chain capacity and physiology in mice with profoundly reduced levels of mitochondrial respirasomes, Cell Metab. 35 (2023) 1799–1813, e1797.
[96] S. Javadov, et al., Mitochondrial respiratory supercomplexes in mammalian cells: structural versus functional role, J. Mol. Med. 99 (2021) 57–73.
[97] L. Yang, et al., Serine catabolism feeds NADH when respiration is impaired, Cell Metab. 31 (2020) 809–821, e806.
[98] G. van der Walt, et al., Sub-cellular metabolomics contributes mitochondria-specific metabolic insights to a mouse model of Leigh syndrome, Metabolites 11 (2021).
[99] K. Esterhuizen, et al., Metabolomics of mitochondrial disease, Mitochondrion 35 (2017) 97–110.
[100] K. Esterhuizen, et al., One mutation, three phenotypes: novel metabolic insights on MELAS, MIDD and myopathy caused by the m.3243A>G mutation, Metabolomics 17 (2021) 10.
[101] K. Esterhuizen, et al., A urinary biosignature for mitochondrial myopathy, encephalopathy, lactic acidosis and stroke like episodes (MELAS), Mitochondrion 45 (2019) 38–45.
[102] C.F. Lee, et al., Targeting NAD(+) metabolism as interventions for mitochondrial disease, Sci. Rep. 9 (2019) 3073.
[103] G. Schleifer, et al., Impaired hypoxic pulmonary vasoconstriction in a mouse model of Leigh syndrome, Am J Physiol Lung Cell Mol Physiol AM J. 316 (2018) L391–L399.
[104] R.M.H. Grange, et al., Hypoxia ameliorates brain hyperoxia and NAD^+ deficiency in a murine model of Leigh syndrome, Mol. Genet. Metab. 133 (2021) 83–93.
[105] N.A. Khan, et al., Effective treatment of mitochondrial myopathy by nicotinamide riboside, a vitamin B3, EMBO Mol. Med. 6 (2014) 721–731.
[106] S. Liu, et al., Glycerol-3-phosphate biosynthesis regenerates cytosolic NAD(+) to alleviate mitochondrial disease, Cell Metab. 33 (2021) 1974–1987.e1979.
[107] K. Majamaa, et al., Metabolic interventions against complex I deficiency in MELAS syndrome, Mol. Cell. Biochem. 174 (1997) 291–296.
[108] Q. Chen, et al., Rewiring of glutamine metabolism is a bioenergetic adaptation of human cells with mitochondrial DNA mutations, Cell Metab. 27 (2018) 1007–1025 (e1005).
[109] J.G. Bogner-Strauss, N-Acetylaspartate metabolism outside the brain: lipogenesis, histone acetylation, and cancer, Front. Endocrinol. 8 (2017) 240.
[110] T.E. Bates, et al., Inhibition of N-acetylaspartate production: implications for 1H MRS studies in vivo, Neuroreport 7 (1996) 1397–1400.
[111] O.A. Lozoya, et al., Mitochondrial nicotinamide adenine dinucleotide reduced (NADH) oxidation links the tricarboxylic acid (TCA) cycle with methionine metabolism and nuclear DNA methylation, PLoS Biol. 16 (2018) e2005707.
[112] I. Martínez-Reyes, N.S. Chandel, Mitochondrial TCA cycle metabolites control physiology and disease, Nat. Commun. 11 (2020) 102.
[113] C. Clarke, et al., Mitochondrial respiratory chain disease discrimination by retrospective cohort analysis of blood metabolites, Mol. Genet. Metab. 110 (2013) 145–152.
[114] M.J. Falk, et al., Metabolic pathway profiling of mitochondrial respiratory chain mutants in *C. Elegans*, Mol. Genet. Metab. 93 (2008) 388–397.
[115] J. Nikkanen, et al., Mitochondrial DNA replication defects disturb cellular dNTP pools and remodel one-carbon metabolism, Cell Metab. 23 (2016) 635–648.
[116] H.M. Liebich, C. Först, Hydroxycarboxylic and oxocarboxylic acids in urine: products from branched-chain amino acid degradation and from ketogenesis, J. Chromatogr. 309 (1984) 225–242.
[117] A.L. Prensky, H.W. Moser, Brain lipids, proteolipids, and free amino acids in maple syrup urine disease, J. Neurochem. 13 (1966) 863–874.
[118] H.M. Liebich, C. Först, Hydroxycarboxylic and oxocarboxylic acids in urine: products from branched-chain amino acid degradation and from ketogenesis, J Chromatogr B Biomed 309 (1984) 225–242.
[119] A.L. Prensky, H.W. Moser, Brain lipids, proteolipids, and free amino acids in maple syrup urine disease, J. Neurochem. 13 (1966) 863–874.
[120] M.M. Heemskerk, et al., Reanalysis of mGWAS results and in vitro validation show that lactate dehydrogenase interacts with branched-chain amino acid metabolism, Eur. J. Hum. Genet. 24 (2016) 142–145.
[121] I. Knerr, et al., Advances and challenges in the treatment of branched-chain amino/keto acid metabolic defects, J. Inherit. Metab. Dis. 35 (2012) 29–40.
[122] E. Treacy, et al., Maple syrup urine disease: interrelations between branched-chain amino-, oxo- and hydroxyacids; implications for treatment; associations with CNS dysmyelination, J. Inherit. Metab. Dis. 15 (1992) 121–135.
[123] J.J. Pink, et al., NAD(P)H:Quinone oxidoreductase activity is the principal determinant of beta-lapachone cytotoxicity, J. Biol. Chem. 275 (2000) 5416–5424.
[124] A. Munnich, et al., Clinical presentations and laboratory investigations in respiratory chain deficiency, Eur. J. Pediatr. 155 (1996) 262–274.
[125] J.-S. Lee, et al., Beta-lapachone, a modulator of NAD metabolism, prevents health declines in aged mice, PloS One 7 (2012) e47122.
[126] S.Y. Lin, et al., Mitochondrial activity is the key to the protective effect of β-Lapachone, a NAD(+) booster, in healthy cells against cisplatin cytotoxicity, Phytomedicine 101 (2022) 154094.
[127] H. Zhang, et al., Distinct metabolic states can support self-renewal and lipogenesis in human pluripotent stem cells under different culture conditions, Cell Rep. 16 (2016) 1536–1547.
[128] J. Zhang, et al., UCP2 regulates energy metabolism and differentiation potential of human pluripotent stem cells, EMBO J. 30 (2011) 4860–4873.
[129] M. Hofer, M.P. Lutolf, Engineering organoids, Nat. Rev. Mater. 6 (2021) 402–420.
[130] K. Thompson, et al., Recent advances in understanding the molecular genetic basis of mitochondrial disease, J. Inherit. Metab. Dis. 43 (2020) 36–50.
[131] F. Pampaloni, et al., The third dimension bridges the gap between cell culture and live tissue, Nat. Rev. Mol. Cell Biol. 8 (2007) 839–845.
[132] Y. Li, K.A. Kilian, Bridging the gap: from 2D cell culture to 3D microengineered extracellular matrices, Adv. Healthc. Mater. 4 (2015) 2780–2796.
[133] S. Thippabhotla, et al., 3D cell culture stimulates the secretion of in vivo like extracellular vesicles, Sci. Rep. 9 (2019) 13012.
[134] K. Aguilar, et al., Microglial response promotes neurodegeneration in the Ndufs4 KO mouse model of Leigh syndrome, Glia 70 (2022) 2032–2044.
[135] A. Quintana, et al., Complex I deficiency due to loss of Ndufs4 in the brain results in progressive encephalopathy resembling Leigh syndrome, Proc. Natl. Acad. Sci. U. S. A. 107 (2010) 10996–11001.
[136] N. Stöberl, et al., Human iPSC-derived glia models for the study of neuroinflammation, J. Neuroinflammation 20 (2023) 231.